Forms of energy dissipated in the damaged zone of of underground cavities: Theoretical analysis and Finite Element Modeling

Hao Xu, Chloé Arson

School of Civil and Environmental Engineering, Georgia Institute of Technology, Atlanta, Georgia 30332, U.S.A.

Abstract

Keywords: Damage model, anisotropic, deviatoric stress, stress path, thermodynamic framework

e

1. Introduction

2. SoA on model of damage inducing irreversible deformation

2.1. damage and plasticity

The first work relating plasticity to damage is introduced by Lubliner [1] in concrete damage model, which defined the damage variable as the ratio of the dissipated plastic energy. In order to ensure the positivity of the damage variable within the framework of the Continuum Damage Mechanics, the damage potential is always proposed as the homogeneous function in terms of damage driving force. Due to the different constrains for the evolution of damage and irreversible strain, in general, the damage potential and the inelastic strain potential are chosen differently, which means the non-associated

flow rule is used in the model. The plasticity theory is coupled to a damage model to reflect the plastic (irreversible) deformation upon unloading [2, 3, 4]. $\mathbb{C}(\mathbf{\Omega}) + \epsilon^p$

2.2. extended CDM

Instead of coupling with the plasticity for permanent strain, the residual strain representing the crack opening after unloading can be taken into account by proposing a damage potential. [5, 6] Enriching the framework of CDM with microscopic properties of geomaterials is another strategy to account for the inelastic strain $\mathbb{C}(\mathbf{\Omega}) + \epsilon^{id}$

2.3. Multiscale strategy

The relationship between fracture mechanics and damage mechanics based on the thermodynamic considerations is built by Mazars & Pijaudier-Cabot [7]. This lead to the equivalent crack concept, in passing from a continuous damage zone to a discrete fracture. Distinct energy terms for the fundamental of cohesive method are studied by Gurtin, and he derived the energy release rate for a sharp crack surrounding by a homogeneous hyperelastic body.

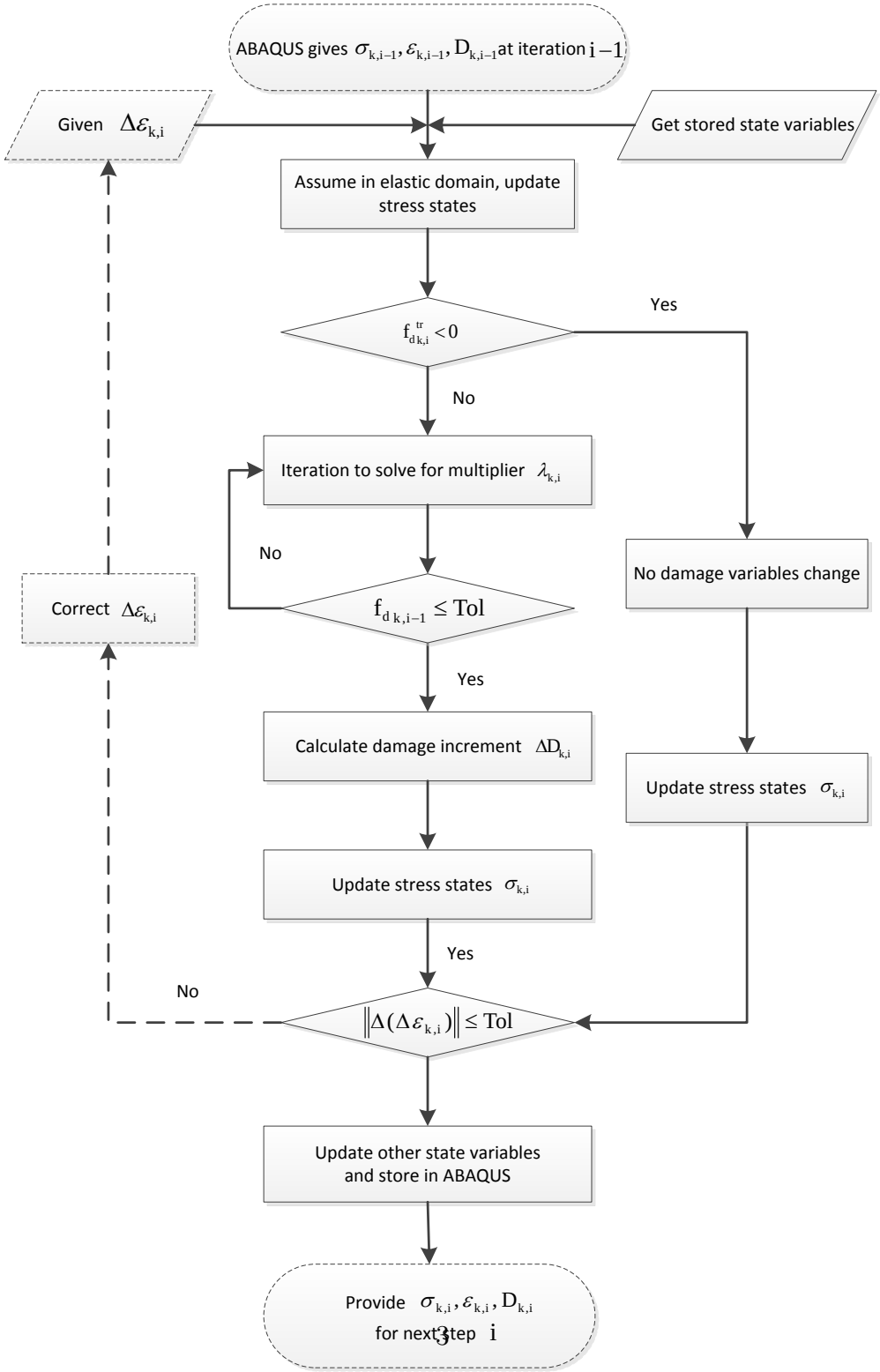

Figure 1: DSID model

2.4. presentation of extended CDM approach (put equations of the model in appendix)

3. Outline of the DSID model

3.1. theoretical framework and algorithms

4. Element Level: analysis of the forms of energy dissipation

4.1. Micro-scopic effects – Energy dissipation

The Inequality of Clausisus-Duhem is derived from the combination of the two first laws of thermodynamics:

$$\dot{\Phi}_s = \boldsymbol{\sigma} : \dot{\boldsymbol{\varepsilon}} - \dot{\psi}_s \geq 0 \tag{1}$$

The free energy rate writes:

$$\dot{\psi}_s = \frac{\partial \psi_s}{\partial \boldsymbol{\varepsilon}^E} : \dot{\boldsymbol{\varepsilon}}^E + \frac{\partial \psi_s}{\partial \boldsymbol{\Omega}} : \dot{\boldsymbol{\Omega}} \tag{2}$$

The dissipation potential of solid skeleton should satisfy the Clausis-Duhem Inequality:

$$\dot{\Phi}_s = \boldsymbol{\sigma} : \dot{\boldsymbol{\varepsilon}}^{id} + \boldsymbol{Y} : \dot{\boldsymbol{\Omega}} \geq 0 \tag{3}$$

The work by the external force is $\boldsymbol{\sigma} : \dot{\boldsymbol{\varepsilon}}$ in each step, and $\dot{\Phi}_s$ is the dissipated energy during each load increment. The strain energy stored in the solid body is $\frac{1}{2}\boldsymbol{\sigma} : \boldsymbol{\varepsilon}^E$. The energy lost in the loading should be always non-negative.

$$\boldsymbol{\sigma} : \dot{\boldsymbol{\varepsilon}}^{id} + \boldsymbol{Y} : \dot{\boldsymbol{\Omega}} \geq 0 \tag{4}$$

4.1.1. Types of energy dissipation

The work by the external force is $\boldsymbol{\sigma} : \dot{\boldsymbol{\varepsilon}}$ in each step, so the accumulate work is $\int \boldsymbol{\sigma} : \dot{\boldsymbol{\varepsilon}} \, \mathrm{d}t$. The accumulate strain energy stored in the solid body is $\frac{1}{2}\boldsymbol{\sigma} : \boldsymbol{\varepsilon}^E$, and the dissipated energy is the differential between the the differential between external work and recoverable strain energy. The mechanical energy lost, $\int \dot{\Phi}_d \, \mathrm{d}t$, in the loading is the area displayed in figure 2 with pink color and should be always non-negative, while the recoverable elastic strain energy is the area of the triangle as figure 2 with light green color.

$$\int \dot{\Phi}_d \, \mathrm{d}t = \int \boldsymbol{\sigma} : \dot{\boldsymbol{\varepsilon}} \, \mathrm{d}t - \frac{1}{2}\boldsymbol{\sigma} : \boldsymbol{\varepsilon}^E \geq 0 \tag{5}$$

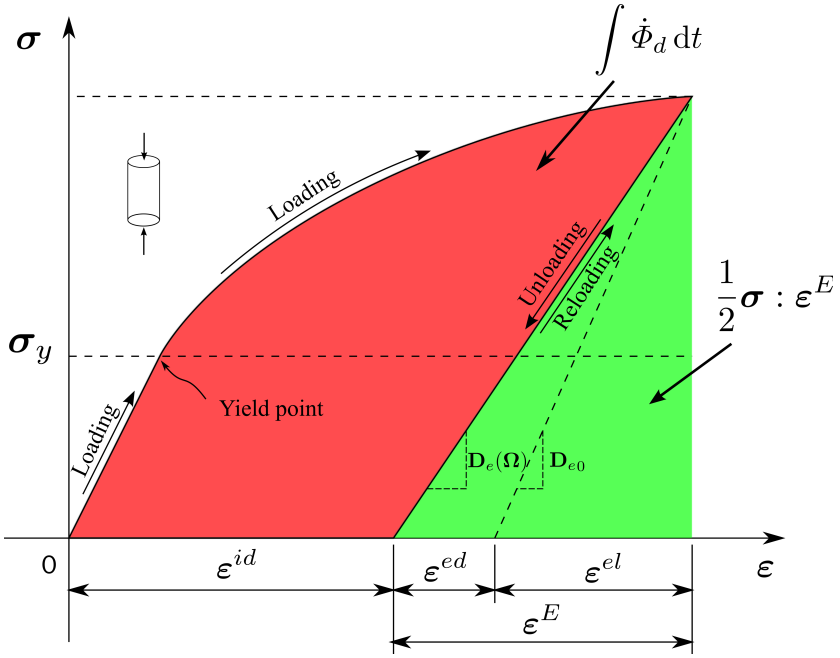

Figure 2: Energy spent in one loading process

The energy dissipated by damage is concluded into two means, crack gener-

ating without additional deformation and debonding paris of crack surfaces. Both of these two approaches can be represented by the mechanical response. Crack generation decrease the stiffness of material, which can increase the capacity that material stores the energy; while debonding is related to non-linear strains. Since there are no other ways of energy transfer (thermal transport or radiation), the energy should be conserved in total. Based on response of material, all of the work by external loading should be splitted into three parts as figure 3 shows (The white part of energy is compensated by the extra part of the energy, related to irreversible strain, above the stress curve). It is also true from the strain decomposition in another side. The energy conservation is expressed as:

$$\int \boldsymbol{\sigma} : \dot{\boldsymbol{\varepsilon}}\, \mathrm{d}t = \int \boldsymbol{\sigma} : \dot{\boldsymbol{\varepsilon}}^{el}\, \mathrm{d}t + \int \boldsymbol{\sigma} : \dot{\boldsymbol{\varepsilon}}^{ed}\, \mathrm{d}t + \int \boldsymbol{\sigma} : \dot{\boldsymbol{\varepsilon}}^{id}\, \mathrm{d}t \tag{6}$$

There are two parts of the energy related to elasto-damage strain, $\boldsymbol{\varepsilon}^{ed}$. Not both of the elasto-damage strain is dissipated, some of them is stored in the solid body as strain energy ($\frac{1}{2}\boldsymbol{\sigma} : \dot{\boldsymbol{\varepsilon}}^{ed}$); the other is dissipated (if material is unloaded), which won't induce the any strain increment. This part noted as $\int \boldsymbol{Y} : \dot{\boldsymbol{\Omega}}\, \mathrm{d}t$ is due to the crack generating but no displacement (figure 4).

$$\int \boldsymbol{\sigma} : \dot{\boldsymbol{\varepsilon}}^{ed}\, \mathrm{d}t = \frac{1}{2}\boldsymbol{\sigma} : \boldsymbol{\varepsilon}^{ed} + \int \boldsymbol{Y} : \dot{\boldsymbol{\Omega}}\, \mathrm{d}t \tag{7}$$

The energy related to debonding of the crack surfaces will be dissipated ($\int \boldsymbol{\sigma} : \dot{\boldsymbol{\varepsilon}}^{id}\, \mathrm{d}t$ related to irreversible strain) or stored ($\frac{1}{2}\boldsymbol{\sigma} : \dot{\boldsymbol{\varepsilon}}^{ed}$, one part of energy related to elasto-damage strain.)

Based on the mechanical part, the lost of the energy is dissipated by the

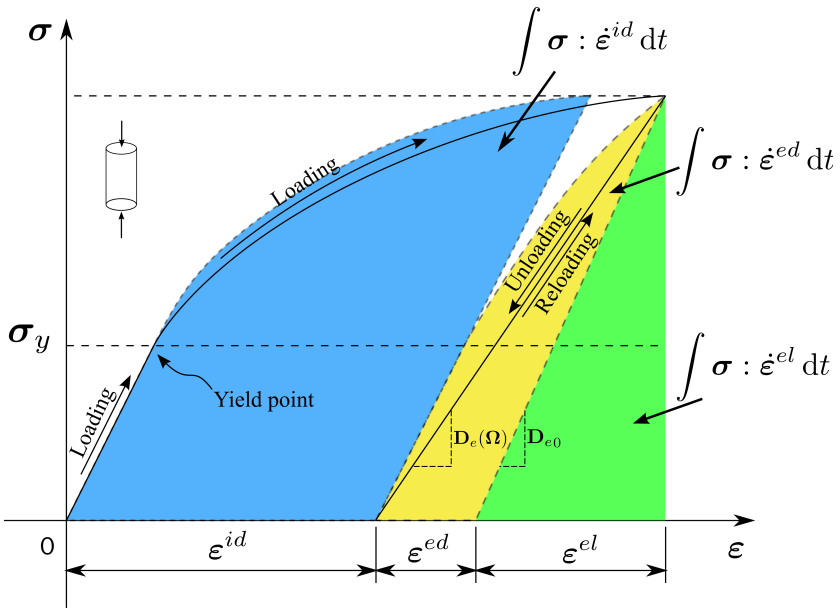

Figure 3: Energy splitting in one loading process

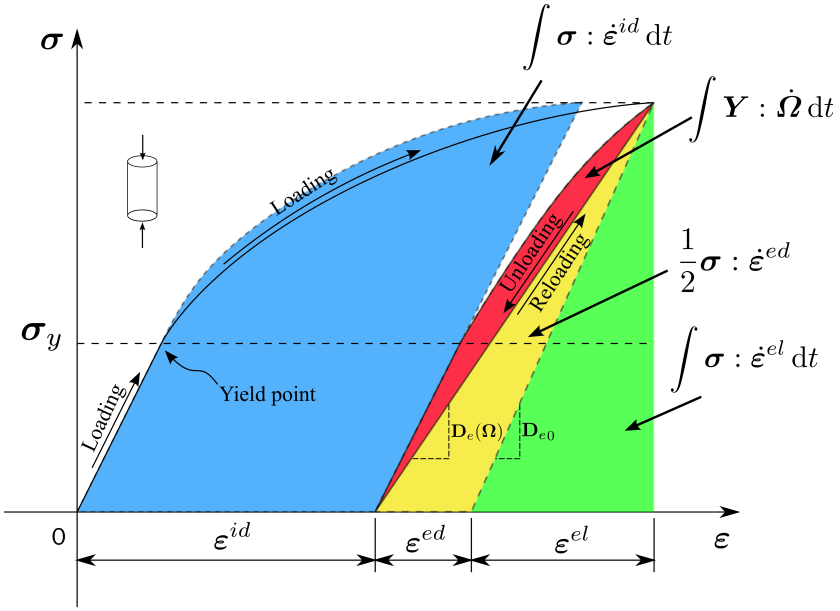

Figure 4: Energy splitting in one loading process

irreversible strain and crack generation due to damage.

$$\int \dot{\Phi}_d \, \mathrm{d}t = \int \boldsymbol{\sigma} : \dot{\boldsymbol{\varepsilon}}^{id} \, \mathrm{d}t + \int \boldsymbol{Y} : \dot{\boldsymbol{\Omega}} \, \mathrm{d}t \geq 0 \tag{8}$$

Therefore, the following equation is hold:

$$\int \boldsymbol{\sigma} : \dot{\boldsymbol{\varepsilon}} \, \mathrm{d}t - \frac{1}{2}\boldsymbol{\sigma} : \boldsymbol{\varepsilon}^E = \int \boldsymbol{\sigma} : \dot{\boldsymbol{\varepsilon}}^{id} \, \mathrm{d}t + \int \boldsymbol{Y} : \dot{\boldsymbol{\Omega}} \, \mathrm{d}t \tag{9}$$

4.2. Limitations of the DSID Model

1. Meso-scopic effects

   The "splitting effects" and "crossing effects" are considered in the DSID model. Both of them follow the Griffth criterion for the mode I failure in rocks. Therefore, the damage generated by pure shear stress and the damage induced by the equivalent principal stress are equal. The equivalence of these two status is lack of the microscopic effects to account for the difference between shear failure and tensile failure.

2. Micro-scopic effects

   Indeedly, the DSID model does not include the failure mechanisms in micro-scale, but the crack debonding is captured by the damage model in terms of the energy. The splitting of the crack surfaces is the micro-scopic effect

Energy dissipation on different types of stress paths.

1. Uniaxial Tensile test

   A uniaxial tensile test is computed with a 100 MPa at element level. After damage threshold, surfaces debonding and irreversible strain dissipate the energy which is input by the external work. In the uniaxial

tensile test, the increase of the percentage of the dissipated energy is apparent. The percentage of the irreversible strain energy increases to 28% and crack debonding spends 12% of the total energy, while the stored elastic energy reduces to about 60%. The energy release rate is high which can infer that the crack propagation in rock under uniaxial tensile is fast and unstable.

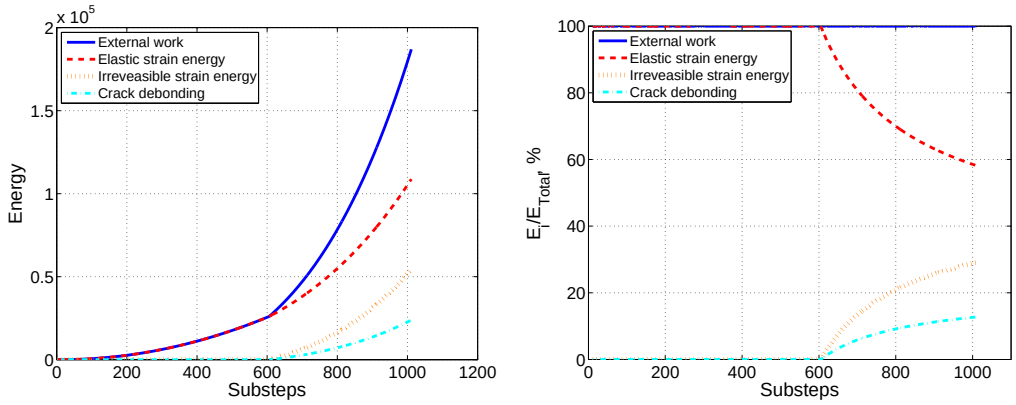

(a) Types of Energy (b) Percentages of Each Energy

Figure 5: Energy in a uniaxial tensile test

2. Shear test need re-calculation and replot

   A pure shear test is simulated with $\sigma_{12} = 60$ MPa pure shear stress. The energy dissipation process is slow (in figure 6, the percentage of the dissipated energy increase insignificantly).

3. Triaxial Compresion test need re-calculation and replot

   A triaxial compression test is computed with a 30 MPa confining stress and a vertical 130 MPa compressive stress. Each energy term in this simulation is summarized as follows.

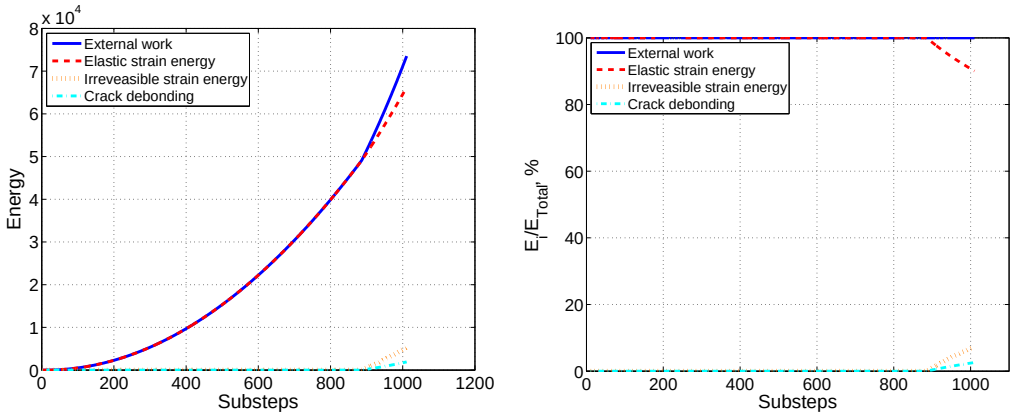

(a) Types of Energy (b) Percentages of Each Energy

Figure 6: Energy in a shear test

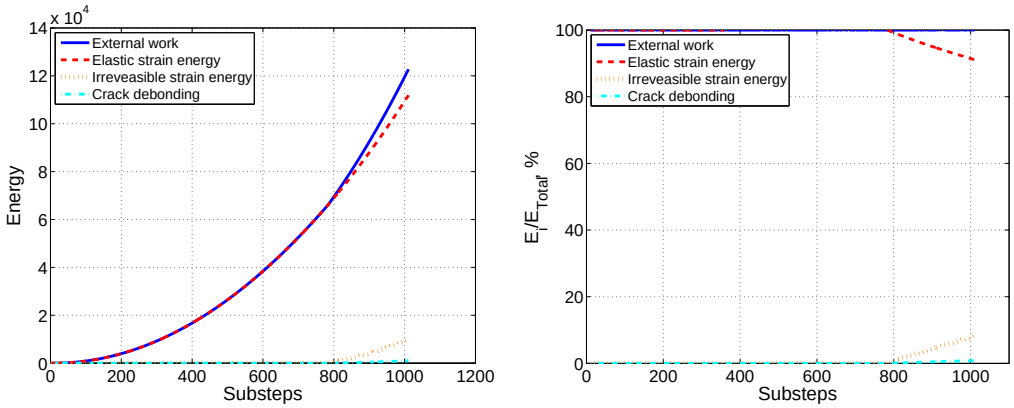

(a) Types of Energy (b) Percentages of Each Energy

Figure 7: Energy in a triaxial compression test

The energy dissipation process in triaxial test is similar as the previous pure shear test, which proofs the mechanism of crack propagation in these two cases are similar. The dissipation of energy is slower than the one in the uniaxial tensile test.

5. FEM simulation of damage dissipation driving propagation

5.1. Energy dissipation during crack propagation

The simulation is computed within a rectangle study domain. The horizontal directions of vertical boundaries are all fixed. The loading is imposed as displacements which are applied on the part of the top and bottom surface. A initial small crack is embedded closed to the left boundary surface. The displacement will induce the crack surface to open and cause the stress concentration around the crack tip, which drives the crack propagates (or damage zone extends) along the x-direction into the rock mass.

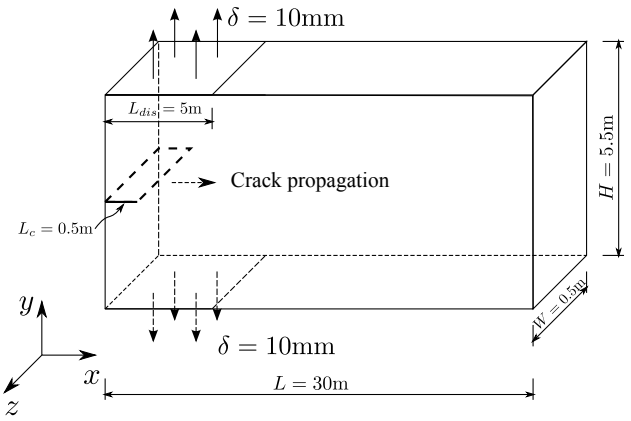

Figure 8: Sketch of the simulation problem.

The dissipated energy in XFEM is:

$$\int \dot{\Phi}_d \, \mathrm{d}t = \int G_c \dot{A} \, \mathrm{d}t \tag{10}$$

If the dissipated energy in different methods is equivalent if input energy to system is equal ???, the relation between these methods can be obtained.

$$\int \boldsymbol{\sigma} : \dot{\boldsymbol{\varepsilon}}^{id} \, \mathrm{d}t + \int \boldsymbol{Y} : \dot{\boldsymbol{\Omega}} \, \mathrm{d}t = \int G_c \dot{A} \, \mathrm{d}t \tag{11}$$

5.2. XFEM

Extended Finite Element Method (XFEM) is a special case of local Partition of Unity Finite Element Method (PUFEM) with extrinsic enrichment. This method is originally developped by .... The idea sustaining XFEM is to add discontinuous enrichment functions to the Finite Element approximation to account for the presence of the crack. The geometry of the cracks is explicitly modeled and finner remeshing is not required. Level set and fast marching methods are used to track moving boundaries.

Enrichment functions.

The enrichment functions typically consist of the near-tip asymptotic functions that capture the singularity around the crack tip and a discontinuous function that represents the jump in displacement across the crack surfaces:

$$\mathbf{u} = \sum_{i=1}^{n} N_i(x)[\mathbf{u}_i + H(x)\mathbf{a}_i + \sum_{\alpha=1}^{4} F_\alpha(x)\mathbf{b}_i^\alpha] \tag{12}$$

where $N_i(x)$ are the usual nodal shape functions; $\mathbf{u}_i$ is the usual nodal displacement vector associated with the continuous part of the finite element solution; the second term is the product of the nodal enriched degree of freedom vector, $\mathbf{a}_i$, and the associated discontinuous jump function $H(x)$ across

the crack surfaces; and the third term is the product of the nodal enriched degree of freedom vector, $\mathbf{b}_i^\alpha$, and the associated elastic asymptotic crack-tip functions, $F_\alpha(x)$.

Cohesive segments method and phantom nodes.

Unlike Cohesive Zone methods, which require that the cohesive surfaces align with element boundaries and the cracks propagate along a set of predefined paths, the XFEM-based cohesive segments method can be used to simulate crack initiation and propagation along an arbitrary, solution-dependent path in the bulk materials. Phantom nodes, which are superposed on the original real nodes, are introduced to represent the discontinuity of the cracked elements. When the element is cut through by a crack, the cracked element splits into two parts. Each phantom node and its corresponding real node are no longer tied together and can move apart. The magnitude of the separation is governed by the cohesive law until the cohesive strength of the cracked element is zero, after which the phantom and the real nodes move independently.

Level set method to describe discontinuous geometry.

A key development that facilitates treatment of cracks in an extended finite element analysis is the description of crack geometry, because the mesh is not required to conform to the crack geometry. The level set method, which is a powerful numerical technique for analyzing and computing interface motion, fits naturally with the extended finite element method and makes it possible to model arbitrary crack growth without remeshing.

The problem is solved by XFEM with fracture energy $G_c = 120\text{N/m}$. The crack is generated within the same plane as initial crack, and propagate along

x-direction (figure 9). The maximum tensile stress occurs at the crack tip with high stress concentration.

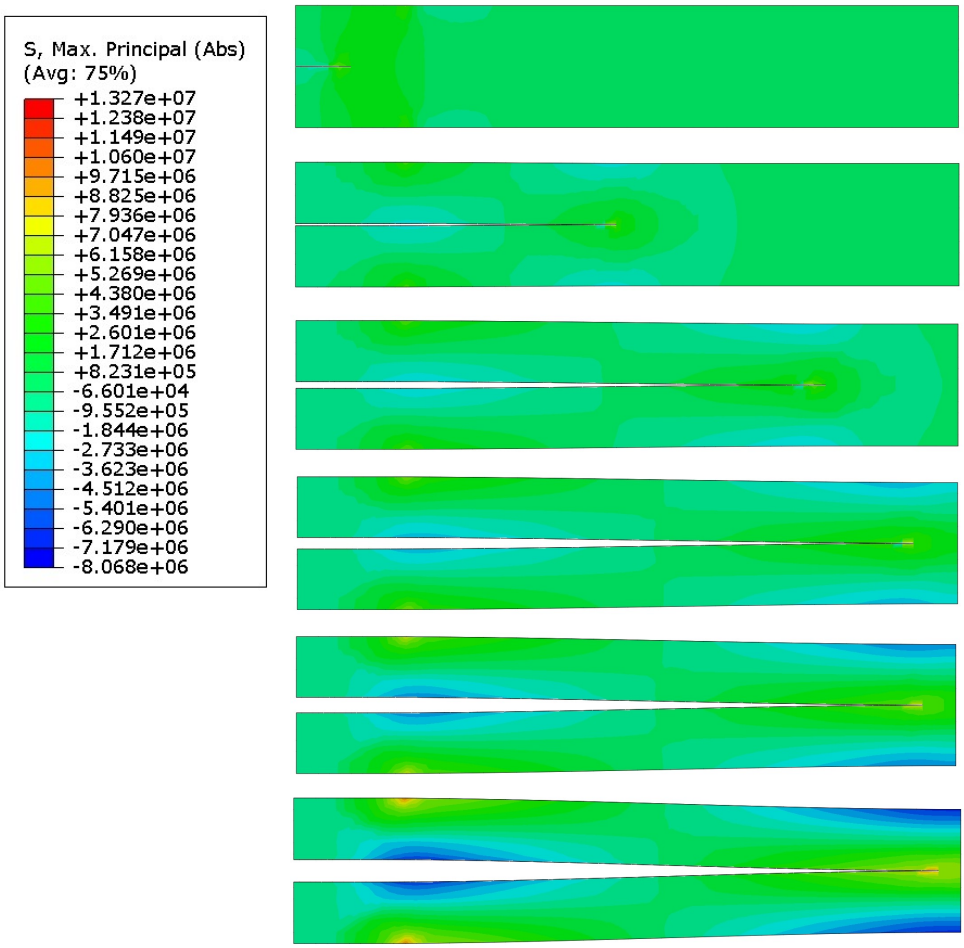

Figure 9: Absolute Maximum Principal Stress distribution during loading processes. The figures are corresponding to the total loading displacement, 0.16, 1.98, 5.98, 10.36, 13.98, and 20 mm. The figure is displayed with 50 amplification factor to show the crack opening.

The total energy is computed as the summation of the elastic energy and dissipated energy in entire domain. The elastic energy is the stress energy

stored in the body of material, while the dissipated energy is the accumulation of the energy released by the crack surface generation. Displayed as the figure 10, when the crack propagates at the very early of the loading, the surface energy dissipate rapidly with the high amount of surface energy releases and the dissipated energy is more than the stored elastic energy. In the physical processes, this is the unstable crack when the initial crack is very small at the beginning, where the catastrophic failure occurs before the full development of a cohesive zone; then the crack propagation slows down, and most of the work is stored into the material as strain energy. Therefore, the elastic energy then increase significantly. The crack propagation is a stable process during the later loading steps with intermediate crack size. The percentage of the elastic energy to the total energy decreases at the occurrence of the crack propagation, then it increases with loading applied; while the dissipated energy is inverse.

The final elastic energy density is illustrated by figure 11. The plot is consistent with the maximum principal distribution in figure 9. The high elastic energy density occurs at the position (boundary edge or crack tip) with the higher tensile stress or compressive stress.

5.3. Cohesive Zone Model

The cohesive zone finite element method, which is originally proposed by Dugdale [8], has been extensively used to simulate fracture and fragmentation processes inconcrete, rock and metals. Similar as XFEM, in order to avoids the singularity in the crack tip stress field that is present in classic

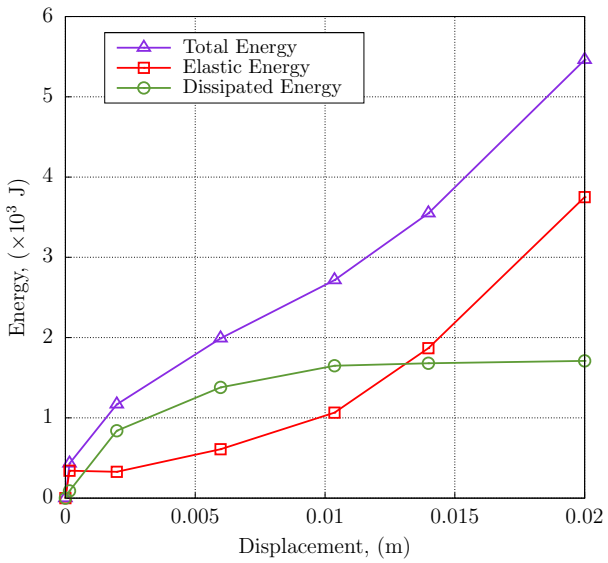

Figure 10: Percentage of the energy evolution during loading steps with XFEM.

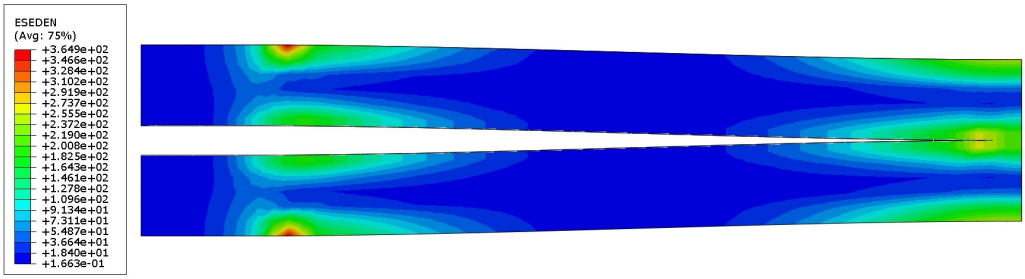

Figure 11: Elastic energy density with XFEM.

fracture mechanics, the cohesive zone model utilizes a simplified fracture process zone characterised by a traction-separation law instead. So the cohesive finite element method provides an alternate, effective approach for quantitative analysis of fracture behaviour through explicit simulation of the fracture processes.

In cohesive-zone models, a stressdisplacement relationship across the crack tip represents the degrading mechanisms in the fracture process zone (add figure). Figure shows the used decohesion relations for quasi-brittle fracture. The cohesive crack tip corresponds to the damage initiation point where the traction reaches the cohesive strength σ_t and the separation reaches the critical value δ_0; the material crack tip is the complete failure point where the separation reaches the critical value δ_f and the traction or cohesive strength acting across the surfaces are equal to zero. The work of separation or fracture energy G_c, which is the work needed to create a unit area of fully developed crack. It is formally defined as

$$G_c = \int \sigma \, \mathrm{d}\delta \tag{13}$$

The same problem is simulated with the fracture energy $G_c = 120\mathrm{N/m}$. The obtained results are different from which are given by XFEM (figure 12), but with similar distribution of maximum principal stress.

Because the dissipated way on energy is assumed by the traction-separation law, the energy dissipates is slower than the simulation by XFEM, and the dissipated energy at beginning is less than the elastic energy. But it still can be found the unstable crack propagation with the small crack size at the beginning. When crack size increase, the surface energy release rate

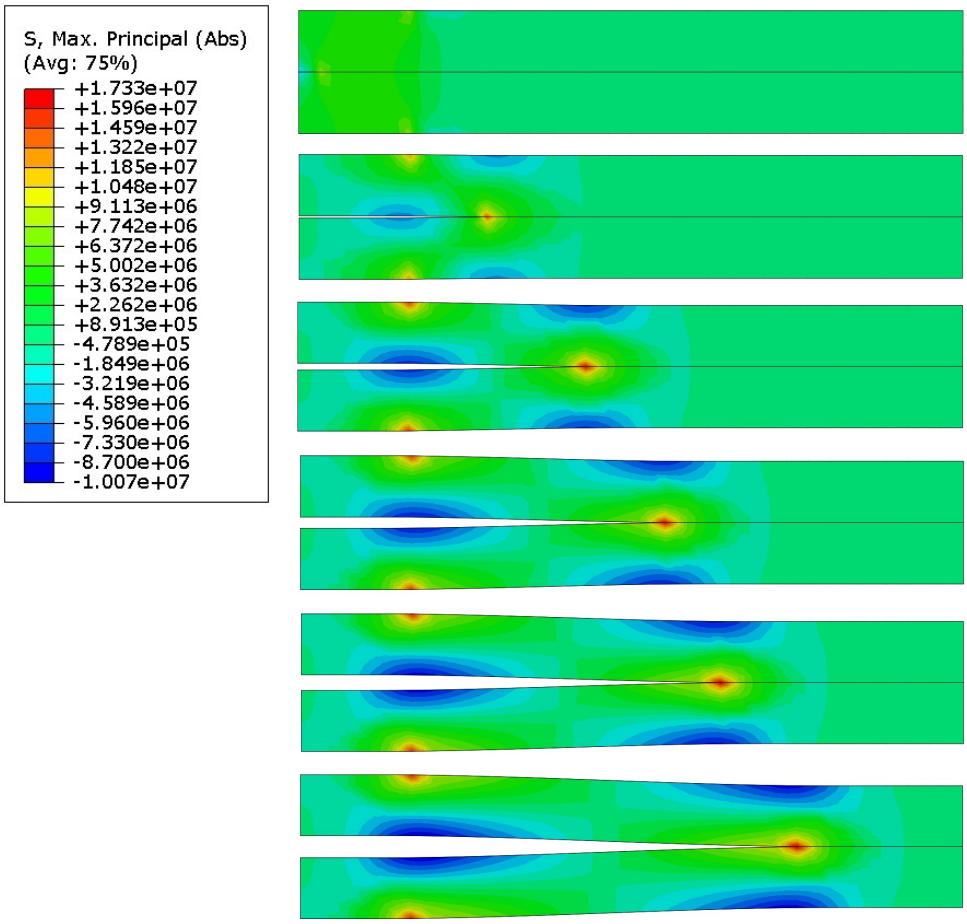

Figure 12: Absolute Maximum Principal Stress distribution during loading processes. The figures are corresponding to the total loading displacement, 0.06, 1.99, 6.00, 9.99, 13.91 and 20 mm. The figure is displayed with 50 amplification factor to show the crack opening.

decrease and most of the work by the external loading is stored as elastic energy. The displacement loading with CZM induces higher energy into the system compared with XFEM. The percentage of the elastic energy to the total energy decreases at the occurrence of the crack propagation, then it increases and almost keep constant with loading growth; while the dissipated energy is inverse.

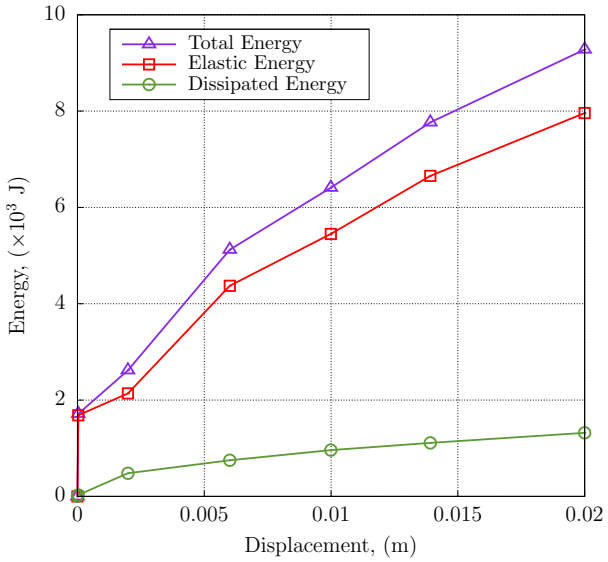

Figure 13: Percentage of the energy evolution during loading steps with CZM.

The final elastic energy density obtained with CZM is displayed in figure 14, in which the energy density distribution consistent with the maximum principal distribution in figure 12. The high elastic energy density occurs at the position (boundary edge or crack tip) with the higher tensile stress or compressive stress, which is the same as the results obtained by XFEM.

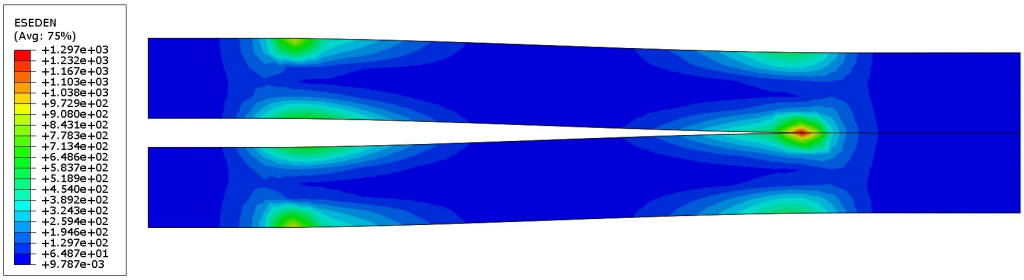

Figure 14: Elastic energy density with CZM.

5.4. Continuum Damage Model

The problem is computed with DSID model, but the damageable elements are only restricted in two layers around in the middle of the entire domain. In this way, the energy can only dissipate along the horizontal layers, so the damage model for crack propagation can be compared with the XFEM and CZM simulations in which the crack plane is restricted horizontally. The other domain is still utilized with elastic material. The results display the tensile zone ahead of the crack tip since the crack tip cannot move. The obtained stress is one order magnitude larger than the previous examples due to the no discontinuity generates and not enough energy releases in this simulation.

The obtained energy in the system is much larger than the previous two examples, in which the energy is 3 order of magnitude less than the DSID model. The energy evolution is more stable than the previous cases. After damage induced, the percentage of the elastic energy decreases with the percentage of the irreversible strain energy and crack debonding energy increase. These three energy terms evolves smoothly in this case, which means that

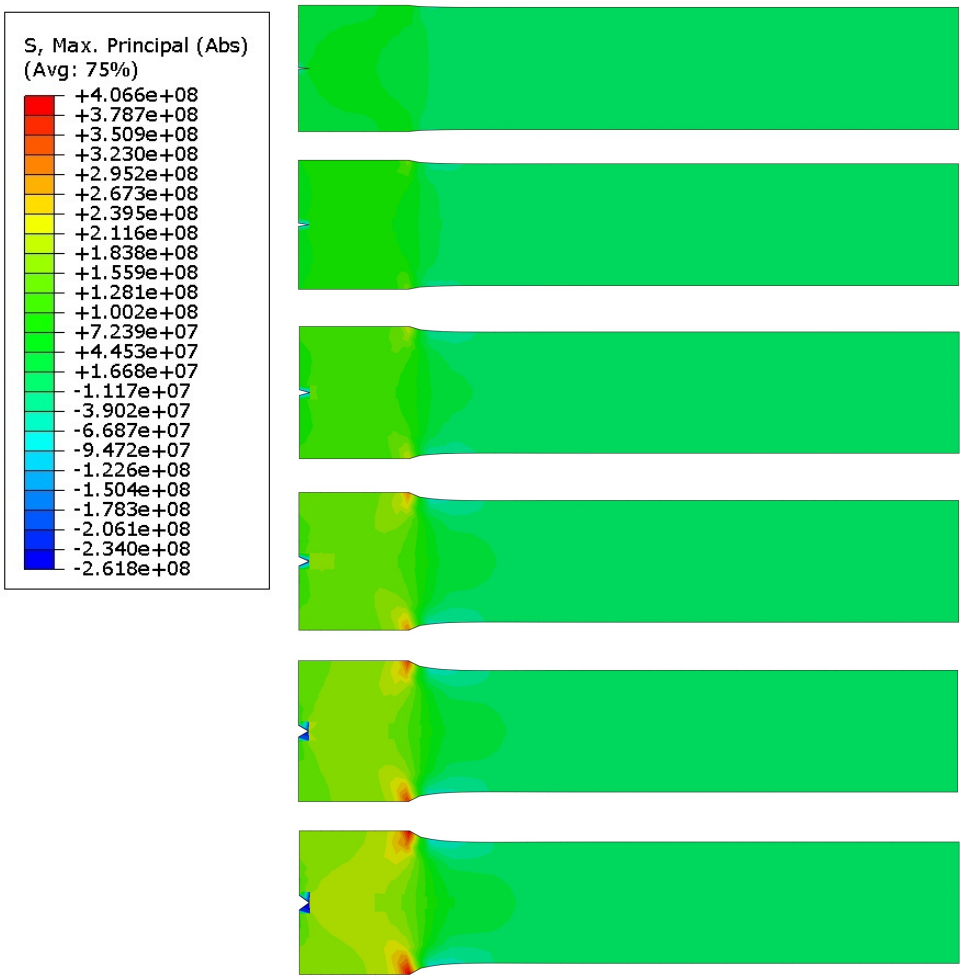

Figure 15: Absolute Maximum Principal Stress distribution during loading processes. The figures are corresponding to the total loading displacement, 3.4, 6.4, 9.8, 14.2, 17, and 20 mm. The figure is displayed with 50 amplification factor to show the crack opening.

microcrack propagation before discontinuity occurs is stable and affects the macroscopic properties smoothly.

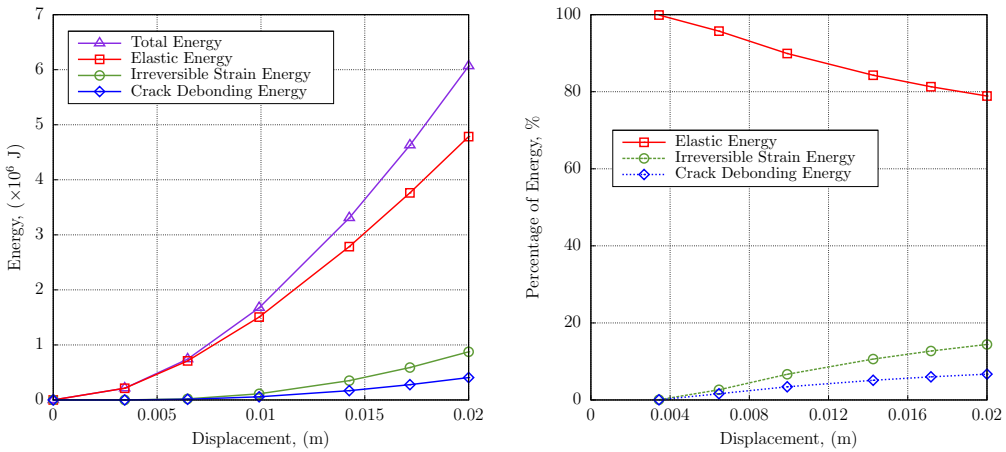

(a) Energy Evolution (b) Percentages of Each Energy

Figure 16: Energy in simulation with DSID Model

The elastic energy density is computed and shows as figure 17. The above figure displays the energy density in elastic domain while the below figure illustrates the ones in damageable domain.

5.5. Comparison between models

To compare the energy consume in DSID model and XFEM, the evolution of the percentage of the elastic energy within the entire study domain is plotted in figure 18. Although the magnitude of the energy are not the same order, but the percentage of the elastic energy illustrates the way how energy evolve during loading growth. Both XFEM and CZM include the discontinuity

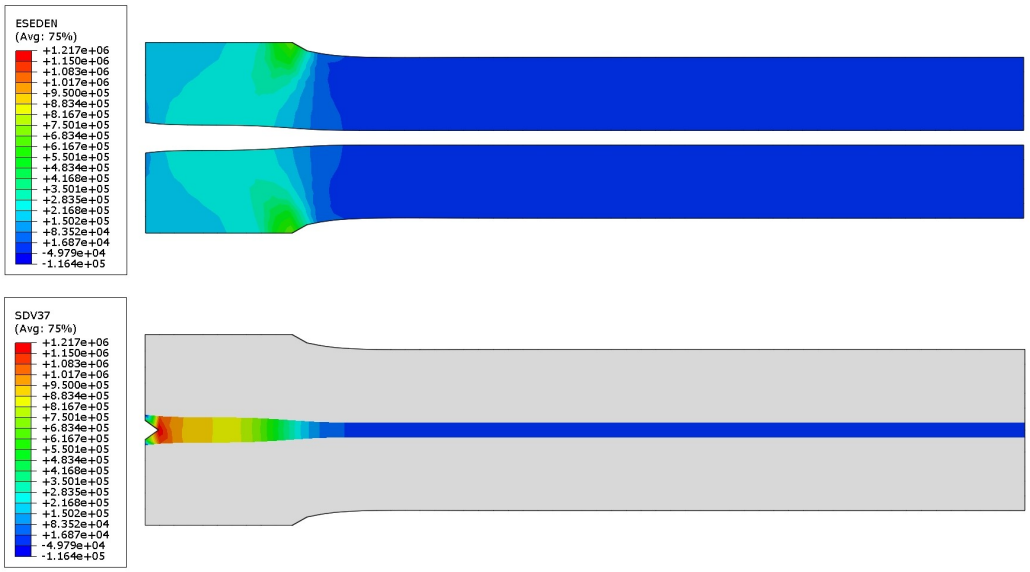

Figure 17: Elastic energy density with DSID.

generation, so the results by XFEM shows the percentage of the elastic energy reduces rapidly when crack starts to propagate which means macro-scopic discontinuity grows unstably. Till the energy percentage reaches a turning point, the crack extension slows down and opening of crack is dominant. Most of the external work is stored by the material after this turning point, so the percentage of the elastic energy increases. However, this phenomenon cannot be captured by continuum model. DSID considers damage as the micro-crack growth, so it still use continuum method to account for the crack evolution without embedding the real discontinuity. This way triggers the crack propagate gently so that the material properties decreases smoothly.

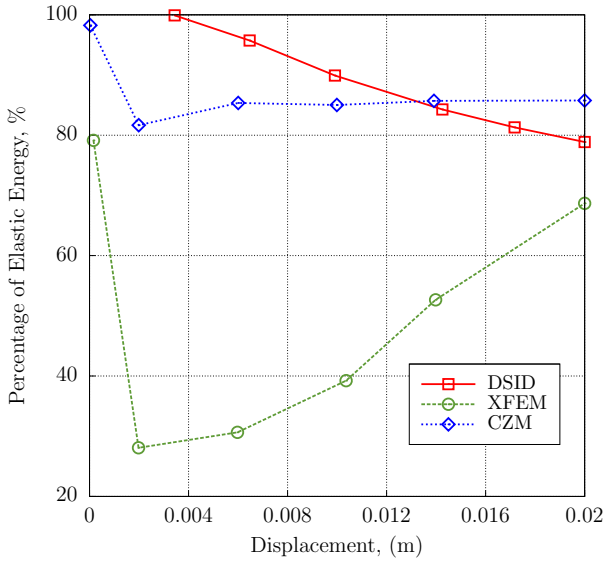

Figure 18: Percentage of the elastic energy during loading steps.

6. Conclusion

Acknowledgments

This study was conducted at the Georgia Institute of Technology, as part of a research program on Finite Element Modeling of Hydraulic Fracturing. Funding was provided by ConocoPhillips, Houston, Texas.

Appendix A. The DSID Model

Appendix A.1. Outline of the DSID Model

For instance, [2] and [3] used a second-order damage tensor in a free energy potential expressed in terms of elastic strains, while [4] adopted the same approach with a different free energy expressed in terms of elastic strain and modified strains. However elastic strains cannot be controlled as such in

an experiment of as a boundary condition in a numerical code. That is the reason why [5] and [6] expressed rock skeleton free energy in terms of total strains. Their model turned out to be easier to calibrate against experimental data. [9] and [10] employed a similar strategy, with the additional use of a parameter expressing the degree of anisotropy, allowing accounting for non-orthotropic damage. In uniaxial compression for instance, cracks can develop both parallel to the axis (orthotropic component of damage) and perpendicular to the axis (isotropic component of damage). An anisotropic damage model based on a stress-dependent free energy potential was proposed by [11]; [12], [13] and [14]. [14] used a modified stress tensor to account for the difference between compressive and tensile stress. The damage evolution law derives from a criterion expressed in terms of the energy release rate conjugate to damage. In the former models on the contrary, damage evolution law is not derived from the damage potential with the energy release rate that is conjugate to damage: damage rate is calculated using associated variables used to predict crack lengths. Differences between the afore-mentioned damage models are highlighted in Table A.1.

Most anisotropic damage models for geomaterials postulate a skeleton free energy expressed in terms of deformation. As a result, the energy release rate $\mathbf{Y}$ (also called damage driving force) conjugate to damage is also a function of deformation. In order to capture cracks due to "splitting effects" (i.e. Griffith cracks) and equivalent cracks due to "crossing effects" (i.e. wing shear cracks), it is necessary to make the damage criterion depend on a tensile damage driving force. In order to better account for states of tensile deformation under differential stress, the proposed anisotropic dam-

Models	Free energy	Damage criterion or damage evolution law	Driving force	Stress Variables	Strain Variabless
[2, 3]	$\psi_s(\boldsymbol{\varepsilon}^e, \boldsymbol{\phi}^{\pm}, \varepsilon_{eq}^{\pm}, \phi_{eq}^{\pm})$ $= \psi^e(\boldsymbol{\varepsilon}^e, \boldsymbol{\phi}^{\pm}) + \Psi^p(\varepsilon_{eq}^{\pm}) + \psi^d(\phi_{eq}^{\pm})$	$f_d^{\pm}(\boldsymbol{Y}^{\pm}, \phi_{eq}^{\pm})$	$\boldsymbol{Y}^{\pm}$	$\boldsymbol{\sigma}^{\pm}$	$\boldsymbol{\varepsilon}^e$ and $\boldsymbol{\varepsilon}_{eq}$
[4]	$\psi_s = \psi^e(\boldsymbol{\varepsilon}^e, \boldsymbol{\Omega}) + \psi^d(\beta)$	$f_d(\boldsymbol{Y}, \beta)$	$\boldsymbol{Y}$		$\boldsymbol{\varepsilon}^e$ and $\bar{\boldsymbol{\varepsilon}}^e$
[5, 6]	$\psi_s(\boldsymbol{\varepsilon}, \boldsymbol{\Omega})$	$f_d(\boldsymbol{Y}^+, \boldsymbol{\Omega})$	$\boldsymbol{Y}^+ = g\boldsymbol{\varepsilon}^+$		$\boldsymbol{\varepsilon}$ and $\boldsymbol{\varepsilon}^{\pm}$
[9]	$\psi_s(\boldsymbol{\varepsilon}, d_i)$	$\boldsymbol{Q}^* = (1-\xi)\boldsymbol{I} + \xi\boldsymbol{\Gamma}^*$ $\dot{\boldsymbol{\Omega}} = \dot{\mu}\mathbb{Q}^*$	$\boldsymbol{Y}$		$\boldsymbol{\varepsilon}$
[10]	$\psi_s(\boldsymbol{\varepsilon}^e, p, \boldsymbol{\Omega})$	$\dot{\boldsymbol{\Omega}} = \mathbb{S} : \boldsymbol{Y}$ $\mathbb{S} = (\beta-1)\mathbb{I} + \boldsymbol{I} \otimes \boldsymbol{I}$	$\boldsymbol{Y}$	$\boldsymbol{\sigma}$ and effective stress $\hat{\boldsymbol{\sigma}}$	$\boldsymbol{\varepsilon}^e$
[11, 12, 13]	$\psi_s(\boldsymbol{\sigma}, \boldsymbol{\Omega})$	based on micro-mechanics concepts	not included		
[14]	$\psi_s(\boldsymbol{\sigma}, r, \boldsymbol{\Omega}, \beta)$	$f_d(\boldsymbol{Y}, r, \boldsymbol{\Omega})$	$\boldsymbol{Y}$	$\boldsymbol{\sigma}$ and $\bar{\boldsymbol{\sigma}}$	

Table A.1: Comparison of Several Model Formulations for Anisotropic Damage.

age model is hyper-elastic, and a free energy potential expressed as a term of stress (Gibbs free energy, G_s) is proposed. This free energy accounts for the surface energy dissipated by opened cracks and closed cracks, and the elastic energy stored in material as well. To stay within the framework of linear elasticity in the absence of damage, the expression of the free energy should have at most quadratic terms of $\boldsymbol{\sigma}$ [5, 11] . The thermodynamic framework of the DSID model is summarized in Table. A.2. Stress/strain relationships are derived from the expression of a free energy potential. Damage evolution is controlled by a damage function, similar to Drucker-Prager yield function (but depending on the energy release rate). The damage flow rule is non-associate, and the damage potential is chosen so as to ensure the positivity of dissipation associated to damage. The irreversible deformation due to damage follows an associated flow rule, which allows representing physical anisotropic trends of the deformation tensor during the damage process. More details are provided in [15].

[1] J. Lubliner, J. Oliver, S. Oller, E. Onate, International Journal of Solids and Structures 23 (1989) 299–326.

[2] R. K. Abu Al-Rub, S.-M. Kim, Engineering Fracture Mechanics 77 (2010) 1577–1603.

[3] U. Cicekli, G. Z. Voyiadjis, R. K. Abu Al-Rub, International Journal of Plasticity 23 (2007) 1874–1900.

[4] S. Murakami, K. Kamiya, Int. J. Mech. Sci. 39 (1996) 473–486.

[5] D. Halm, A. Dragon, Eur. J. Mech. A/ Solids 17 (1998) 439–460.

Table A.2: Thermodynamic framework of the DSID model

D.S.I.D. Model		
Free Energy	$G_s(\boldsymbol{\sigma}, \boldsymbol{\Omega}) = \frac{1}{2}\boldsymbol{\sigma} : \mathbb{S}_0 : \boldsymbol{\sigma} + a_1\,\mathrm{Tr}\boldsymbol{\Omega}(\mathrm{Tr}\boldsymbol{\sigma})^2 + a_2\,\mathrm{Tr}(\boldsymbol{\sigma}\cdot\boldsymbol{\sigma}\cdot\boldsymbol{\Omega})$ $+a_3\,\mathrm{Tr}\boldsymbol{\sigma}\,\mathrm{Tr}(\boldsymbol{\Omega}\cdot\boldsymbol{\sigma}) + a_4\,\mathrm{Tr}\boldsymbol{\Omega}\,\mathrm{Tr}(\boldsymbol{\sigma}\cdot\boldsymbol{\sigma})$	
	$\boldsymbol{\varepsilon}^E = \frac{\partial G_s}{\partial \boldsymbol{\sigma}} = \frac{1+\nu_0}{E_0}\boldsymbol{\sigma} - \frac{\nu_0}{E_0}(\mathrm{Tr}\boldsymbol{\sigma})\,\boldsymbol{\delta} + 2a_1(\mathrm{Tr}\boldsymbol{\Omega}\,\mathrm{Tr}\boldsymbol{\sigma})\,\boldsymbol{\delta} + a_2(\boldsymbol{\sigma}\cdot\boldsymbol{\Omega} + \boldsymbol{\Omega}\cdot\boldsymbol{\sigma})$ $+a_3[\,\mathrm{Tr}(\boldsymbol{\sigma}\cdot\boldsymbol{\Omega})\,\boldsymbol{\delta} + (\mathrm{Tr}\boldsymbol{\sigma})\,\boldsymbol{\Omega}\,] + 2a_4(\mathrm{Tr}\boldsymbol{\Omega})\,\boldsymbol{\sigma}$	
	$\boldsymbol{Y} = \frac{\partial G_s}{\partial \boldsymbol{\Omega}} = a_1(\mathrm{Tr}\boldsymbol{\sigma})^2\,\boldsymbol{\delta} + a_2\boldsymbol{\sigma}\cdot\boldsymbol{\sigma} + a_3\mathrm{Tr}(\boldsymbol{\sigma})\boldsymbol{\sigma} + a_4\mathrm{Tr}(\boldsymbol{\sigma}\cdot\boldsymbol{\sigma})\boldsymbol{\delta}$	
Damage Function	$f_d = \sqrt{J^*} - \alpha I^* - k$	
	$J^* = \frac{1}{2}(\mathbb{P}_1 : \boldsymbol{Y} - \frac{1}{3}I^*\boldsymbol{\delta}) : (\mathbb{P}_1 : \boldsymbol{Y} - \frac{1}{3}I^*\boldsymbol{\delta}), \quad I^* = (\mathbb{P}_1 : \boldsymbol{Y}) : \boldsymbol{\delta}$	
	$\mathbb{P}_1(\boldsymbol{\sigma}) = \sum_{p=1}^{3}\left[H(\sigma^{(p)}) - H(-\sigma^{(p)})\right]\boldsymbol{n}^{(p)}\otimes\boldsymbol{n}^{(p)}\otimes\boldsymbol{n}^{(p)}\otimes\boldsymbol{n}^{(p)}$	
	$k = C_0 - C_1\mathrm{Tr}(\boldsymbol{\Omega})$	
Damage Potential	$g_d = \sqrt{\frac{1}{2}(\mathbb{P}_2 : \boldsymbol{Y}) : (\mathbb{P}_2 : \boldsymbol{Y})}$	
	$\mathbb{P}_2 = \sum_{p=1}^{3} H\left[\max_{q=1}^{3}(\sigma^{(q)}) - \sigma^{(p)}\right]\boldsymbol{n}^{(p)}\otimes\boldsymbol{n}^{(p)}\otimes\boldsymbol{n}^{(p)}\otimes\boldsymbol{n}^{(p)}$	
Flow Rule	$\dot{\boldsymbol{\varepsilon}}^{id} = \dot{\lambda}_d\frac{\partial f_d}{\partial \boldsymbol{\sigma}} = \dot{\lambda}_d\frac{\partial f_d}{\partial \boldsymbol{Y}} : \frac{\partial \boldsymbol{Y}}{\partial \boldsymbol{\sigma}}$	
	$\dot{\boldsymbol{\Omega}} = \dot{\lambda}_d\frac{\partial g_d}{\partial \boldsymbol{Y}}$	
G_s: Gibbs free energy	$\boldsymbol{\sigma}$: Stress tensor	$\boldsymbol{\Omega}$: Damage variable
$\boldsymbol{\varepsilon}^E$: Total elastic strain	ν_0: Poisson's ratio	$\mathbb{S}_0$: Undamaged compliance tensor
E_0: Young's Modulus	$\boldsymbol{\delta}$: Kronecker delta	$\boldsymbol{Y}$: Damage driving force
f_d: Damage function	$\mathbb{P}_1$ and $\mathbb{P}_2$: Projection tensors	$H(\cdot)$: Heaviside function
C_0: Initial damage threshold	g_d: Damage potential	$\max(\cdot)$: Maximum function
$\dot{\boldsymbol{\varepsilon}}^{id}$: Irreavisible strain rate	$\dot{\lambda}_d$: Lagrangian Multiplier	$\dot{\boldsymbol{\Omega}}$: Damage rate
$a_1,\ a_2,\ a_3,\ a_4$: Material parameters	$\sigma^{(p)}$ and $\boldsymbol{n}^{(p)}$: Principal stress and corresponding direction	C_1: Damage hardening variable

[6] F. Homand-Etienne, D. Hoxha, J. F. Shao, Computers and Geotechnics 22 (1998) 135–151.

[7] J. Mazars, G. Pijaudier-Cabot, International Journal of Solids and Structures 33 (1996) 3327–3342.

[8] D. S. Dugdale, J. Mech. phys. Solids 8 (1960) 100–104.

[9] J.-L. Chaboche, International Journal of Damage Mechanics 2 (1993) 311–329.

[10] F. Pellet, A. Hajdu, F. Deleruyelle, F. Besnus, Int. J. Numer. Anal. Meth. Geomech. 29 (2005) 941–970.

[11] J. Shao, H. Zhou, K. Chau, International Journal for Numerical and Analytical Methods i Geomechanics 29 (2005) 1231 – 1247.

[12] J. F. Shao, K. T. Chau, X. T. Feng, International Journal of Rock Mechanics & Mining Sciences 43 (2006) 582–592.

[13] J. Zhou, J. Shao, W. Xu, Mechanics Research Communications 33 (2006) 450–459.

[14] K. Hayakawa, S. Murakami, International Journal of Damage Mechanics 6 (1997) 333–363.

[15] H. Xu, C. Arson, International Journal of Computational Methods, Special Issue on Computational Geomechanics 11 (2014).